

3D Bivariate Spatial Modelling of Argo Ocean Temperature and Salinity Profiles

Mary Lai O. Salvaña¹, Jian Cao², and Mikyoung Jun³

July 15, 2025

Abstract

Variables contained within the global oceans can detect and reveal the effects of the warming climate, as the oceans absorb huge amounts of solar energy. Hence, information regarding the joint spatial distribution of ocean variables is critical for understanding the climate. In this paper, we investigate the spatial dependence structure between ocean temperature and salinity using data harvested from the Argo program and construct a bivariate spatial model for the data that cover the surface to the ocean's interior. We develop a flexible class of multivariate nonstationary covariance models defined in 3-dimensional (3D) space (longitude \times latitude \times depth) that allow the variances and correlation to vary with ocean depth. These models describe the joint spatial distribution of the two variables while incorporating the underlying vertical structure of the ocean. We apply this framework to temperature and salinity data from Argo floats. To manage the computational challenges posed by the large volume of the Argo data, we apply the Vecchia approximation to the likelihood functions. We demonstrate that the proposed bivariate covariance is able to describe the complex vertical cross-covariance structure between the original processes as well as their first and second-order differentiations, while existing bivariate models, including bivariate Matérn, poorly fit the empirical cross-covariance structure.

Some key words: 3D covariance functions; Argo; cross-covariance function; nonstationary; salinity; spatial; temperature.

¹Department of Statistics, University of Connecticut, Email: marylai.salvana@uconn.edu

²Department of Mathematics, University of Houston, Email: jcao21@central.uh.edu

³Corresponding author. Department of Mathematics, University of Houston, Email: mjun@central.uh.edu
Mikyoung Jun acknowledges support by NSF DMS-1925119, DMS-2105847, and DMS-2413042. The authors also acknowledge helpful discussions with Mikael Kuusela on Argo data.

1 Introduction

The international scientific program named Array for Real-time Geostrophic Oceanography (ARGO) was launched in the early 2000s as a response to the call for global observation networks to monitor the climate system (Argo, 2000; Johnson et al., 2022). Since then, the program has launched a global network of 4,000 free-drifting Argo profiling floats that measure ocean variables in the upper 2,000 meters of the world’s oceans. Each float performs a ten-day “park-and-profile” mission. From the surface, the float descends to the drift depth at 1,000 meters where it will park for nine days. At the tenth day, the float descends to 2,000 meters and collects temperature (in degree Celsius or $^{\circ}\text{C}$), salinity (in practical salinity unit or PSU), and pressure (in decibar or dbar) measurements as it ascends to the surface. Once at the surface, the data collected are transmitted via satellite. The full “park-and-profile” mission is illustrated in Figure 1. The data harvested by the floats are made available within 24 hours of their collection as Argo data products (<https://argo.ucsd.edu>). By making the data publicly accessible, the Argo program offers the research community opportunities and challenges to analyze ocean processes.

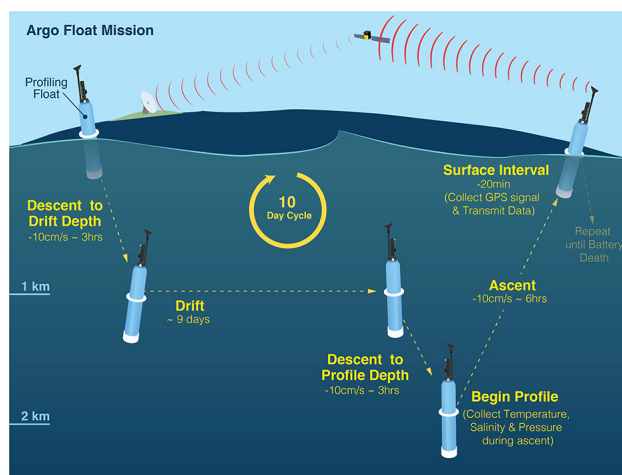


Figure 1: Standard Argo “park-and-profile” mission (Source: Wong et al. (2020))

The core Argo data products are temperature and salinity measurements, the two most important variables through which other oceanographic variables—such as freezing point, electrical conductivity, and viscosity (Pawlowicz, 2013); ocean heat content and potential density (Yarger

et al., 2022); and tropical cyclone-induced ocean thermal response (Hu et al., 2020)—can be derived. Temperature and salinity have been key to understanding the physical properties and dynamics of the ocean. Their distributions have been shown to drive ocean circulation (Chen et al., 2022; Gangopadhyay, 2022), affect climate processes (Olson et al., 2022), and change biogeochemistry (Galán et al., 2021; Ding et al., 2022). They have also been used to study hydroacoustic sound propagation (Jana et al., 2022), design offshore wind farms (Escobar et al., 2016), and identify stressors to organisms in seawater and freshwater (Walker et al., 2020).

1.1 Spatial Interpolation of Argo Data

Spatially continuous maps of temperature and salinity measurements are essential to multidisciplinary scientific research. However, despite the planetary scale and subsurface reach of the Argo profiling network, not all locations are sampled. Since other ocean variables depend heavily on temperature and salinity, efforts are focused on obtaining the best interpolated maps of these two variables. Several institutions have produced high-resolution, gridded global temperature and salinity datasets from the sparse measurements recorded by the Argo floats using various interpolation techniques (Liu et al., 2020a). The list includes the EN4 dataset from the U.K. Met Office (Good et al., 2013) and the grid point values of the Monthly Objective Analysis using Argo data (MOAA) from the Japan Agency for Marine-Earth Science and Technology (JAMSTEC) (Hosoda et al., 2008). Another example is the Barnes Objective Analysis Argo (BOA-Argo) gridded dataset, which employs objective interpolation based on Barnes successive correction method (Li et al., 2017).

One of the most highly used Argo data product is the Roemmich–Gilson Argo climatology from the Scripps Institution of Oceanography (Roemmich and Gilson, 2009). They used weighted local regression in its high-resolution global mapping. Suppose $\mathbf{s} = (L, l, p)^\top$ is the spatial location vector, where L denotes latitude, l denotes longitude, and p denotes pressure (in decibars). While Argo floats measure pressure directly, it is common practice in oceanographic literature

to refer to it as depth, since pressure increases approximately linearly with depth in the upper ocean. For clarity, in this paper, and in various Argo studies, p is treated as a vertical coordinate representing depth, recognizing that it is actually recorded as pressure. Let t denote time, measured in yeardays (days since January 1 of a given year). For $\mathbf{s}_0 = (L_0, l_0, p_0)^\top$, a reference spatial location vector, and t_0 , the reference time index, Roemmich and Gilson (2009) fit the mean function:

$$\begin{aligned} \mu_{\mathbf{s}_0, t_0}(\mathbf{s}, t) = & \beta_0 + \beta_1(L - L_0) + \beta_2(l - l_0) + \beta_3(L - L_0)^2 + \beta_4(l - l_0)^2 + \beta_5(p - p_0) + \beta_6(p - p_0)^2 \\ & + \sum_{k=1}^6 \gamma_k \sin\left(2\pi k \frac{t}{365.25}\right) + \sum_{k=1}^6 \delta_k \cos\left(2\pi k \frac{t}{365.25}\right) \end{aligned} \quad (1)$$

to measurements from the sampled location (L, l, p) , such that (L, l) is one of the 100 nearest neighbors from (L_0, l_0) , for t within 12 calendar months from t_0 , and for p which is one pressure level above or below p_0 . Here, β_0 and β_k , γ_k , and δ_k , $k = 1, \dots, 6$, are scalar coefficients. Furthermore, they modelled the residuals using the spatial covariance function:

$$C(L_1, L_2; l_1, l_2) \propto 0.77 \exp\left[-\left\{\frac{h_{\text{RG}}(L_1, L_2; l_1, l_2)}{140 \text{ km}}\right\}^2\right] + 0.23 \exp\left\{-\frac{h_{\text{RG}}(L_1, L_2; l_1, l_2)}{1111 \text{ km}}\right\}, \quad (2)$$

where $h_{\text{RG}}(L_1, L_2; l_1, l_2)$ is a distance function of the form:

$$h_{\text{RG}}(L_1, L_2; l_1, l_2) = \sqrt{(L_1 - L_2)^2 + (l_1 - l_2)^2 + \text{penalty}(L_1, L_2; l_1, l_2)^2}.$$

Here, the penalty term introduces additional distance when the shortest path between two locations crosses dynamic oceanographic features such as barotropic potential vorticity contours or abrupt depth changes, effectively reducing spatial correlation across such physical boundaries. Kuusela and Stein (2018) improved the modelling of the residuals by using an anisotropic exponential space-time covariance function, i.e.,

$$C(L_1, L_2; l_1, l_2; t_1, t_2) = \sigma^2 \exp\{-h_{\text{KS}}(L_1, L_2; l_1, l_2; t_1, t_2)\}, \quad (3)$$

where $\sigma^2 > 0$ is a variance parameter and $h_{\text{KS}}(L_1, L_2; l_1, l_2; t_1, t_2)$ is a new distance function that captures anisotropy:

$$h_{\text{KS}}(L_1, L_2; l_1, l_2; t_1, t_2) = \sqrt{\left(\frac{L_1 - L_2}{\theta_{\text{lat}}}\right)^2 + \left(\frac{l_1 - l_2}{\theta_{\text{lon}}}\right)^2 + \left(\frac{t_1 - t_2}{\theta_t}\right)^2}.$$

Here, $\theta_{\text{lat}} > 0$, $\theta_{\text{lon}} > 0$, and $\theta_t > 0$ are range parameters for the latitude, longitude, and time dimensions, respectively.

Previous studies typically discretize the vertical domain of Argo data into distinct pressure levels, performing high-resolution spatial interpolation separately for each layer. Due to the irregular vertical sampling of Argo profiles, these approaches first interpolate measurements to fixed pressure levels before fitting their proposed mean and covariance functions. For more detailed discussion of these interpolation methods, see Kuusela and Stein (2018) and Hu et al. (2020). However, this extra preprocessing step can introduce significant errors into the model. To address this problem, Yarger et al. (2022) proposed treating the Argo profile data as functional data that changes with pressure and introduced a functional model for the mean of the form:

$$\begin{aligned} \mu_{L_0, l_0, t_0}(L, l, p, t, y) = & \sum_{\tilde{y}=2007}^{2016} \beta_{0, \tilde{y}}(p) \mathbb{1}_{(y=\tilde{y})} + \beta_1(p)(L - L_0) + \beta_2(p)(l - l_0) \\ & + \beta_3(p)(L - L_0)^2 + \beta_4(p)(l - l_0)^2 + \beta_5(p - p_0) + \beta_6(p - p_0)^2 \\ & + \sum_{k=1}^6 \gamma_k \sin\left(2\pi k \frac{t}{365.25}\right) + \sum_{k=1}^6 \gamma_k \cos\left(2\pi k \frac{t}{365.25}\right). \end{aligned} \quad (4)$$

Here, y denotes the year the measurement was obtained, $\mathbb{1}_{(\cdot)}$ is an indicator function, and $\beta_{0,y}(p)$ and $\beta_k(p)$, $k = 1, \dots, 6$, are functions that describe how the coefficients change along pressure. Similar to the mean function in (1), the functional mean (4) is fitted to the measurements from the nearest neighbors. This functional data approach reports lower prediction errors than the pressure-by-pressure approach. The residuals from Yarger et al. (2022) were then modelled using functional principal components.

Commonly, literature on Argo temperature and salinity variables, including the aforementioned studies, model the two variables separately. In this work, we jointly model the temperature

and salinity residuals to include their spatial cross-correlation. Furthermore, the proposed bivariate model in 3D space provides sufficient expressiveness across depth that is suitable for capturing complex oceanographic structures. The ocean, as a fluid, has a density that is a continuous function of depth. This density variation dictates the layering of the ocean waters, or ocean stratification, which is a phenomenon that occurs when different types of water are mixed, e.g., low-temperature and low-salinity subarctic water, high-temperature and high-salinity subtropical water (Sambe and Suga, 2022). Because temperature and salinity are properties of the water-body, ocean stratification can affect their distributions. Bivariate spatial models that account for the ocean’s structure in the vertical dimension may provide a better description of the processes involved.

The rest of the paper is structured as follows: Section 2 describes the data used in the analysis and provides various empirical results. Section 3 introduces the models for the 3D bivariate spatial modelling and discusses computational aspects. Section 4 presents the results of model fitting and prediction, along with model diagnostics. Section 5 concludes the paper.

2 Background

We aim to uncover the spatial relationship between the temperature and salinity residuals obtained by Yarger et al. (2022) so that a clear understanding of the dynamics between temperature and salinity can be achieved. Accomplishing such a task can enable one to visualize the vertical structure of the ocean that is not directly observable and to exploit their spatial relationship for prediction at locations with no measurements.

Top panels in Figures 2 and 3 display values of the temperature and salinity residuals, respectively, at the surface for January-March 2016. We marked six *reference locations* (RL), namely RL1: $(30^{\circ}S, 150^{\circ}W)$, RL2: $(60^{\circ}N, 180^{\circ}W)$, RL3: $(30^{\circ}N, 150^{\circ}W)$, RL4: $(30^{\circ}N, 30^{\circ}W)$, RL5: $(30^{\circ}S, 20^{\circ}W)$, and RL6: $(20^{\circ}S, 80^{\circ}E)$, for subsequent analyses. These six locations are chosen to represent distinct ocean gyres, such as North and South Pacific, North and South Atlantic, and

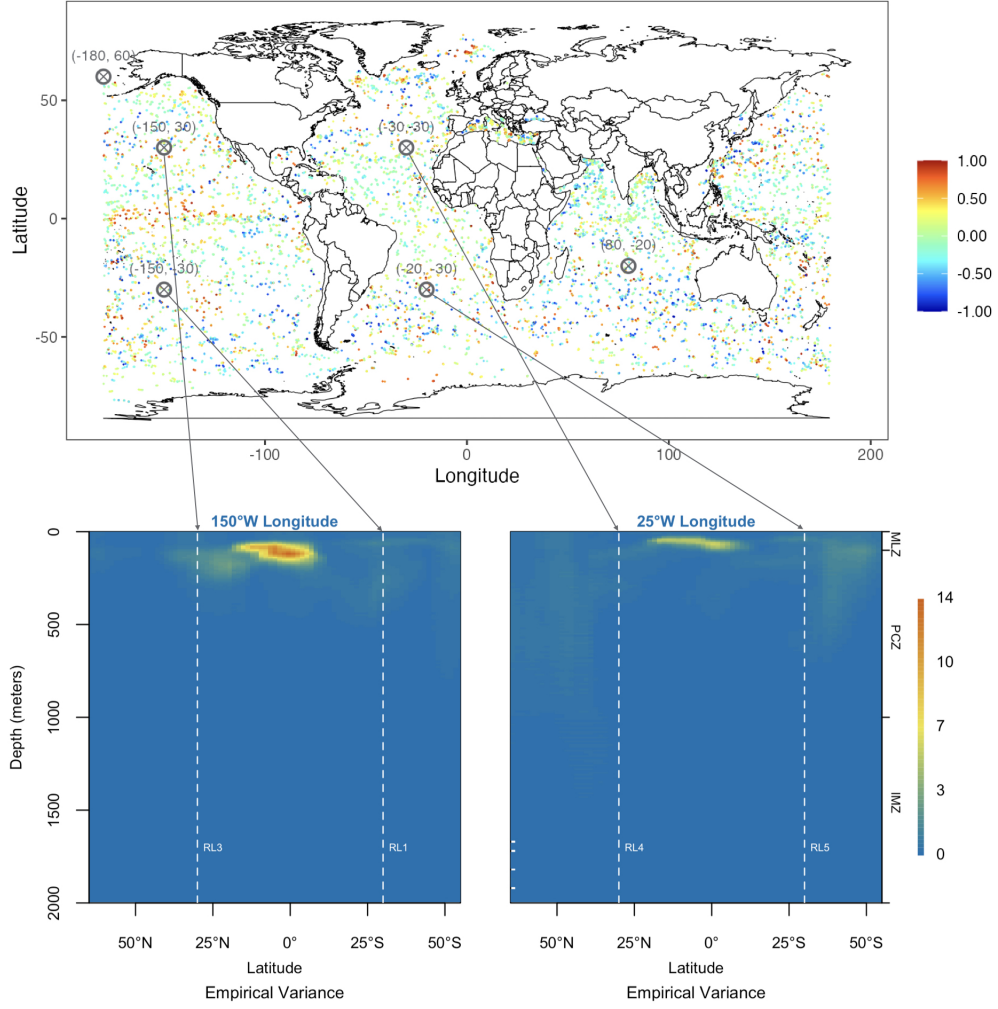


Figure 2: Temperature residuals from January to March in 2016 obtained by Yarger et al. (2022). (Top) Six reference locations are marked with their coordinates. (Bottom) Empirical variances at every 10-meter depth interval along two selected longitude transects: 150°W and 25°W. These transects were chosen because they intersect the most number of reference locations while avoiding land crossings, allowing for a continuous vertical slice of the ocean to be examined. The latitudes of the closest reference locations along each transect are delineated with dashed lines and labeled accordingly.

the Indian Ocean. The boundaries of ocean stratification are also indicated: MLZ for the mixed layer zone at 0–100 meters depth, PCZ for the pycnocline zone at 100–1,000 meters depth, and IMZ for the intermediate zone at 1,000–2,000 meters depth, also referred to as the deep layer (Chen and Geng, 2019). Note that pressure measured in dbar and depth measured in meters are approximately equal, i.e., 1 dbar is approximately 1 meter in depth.

There is no immediately striking pattern of spatial dependence in the surface residuals, except

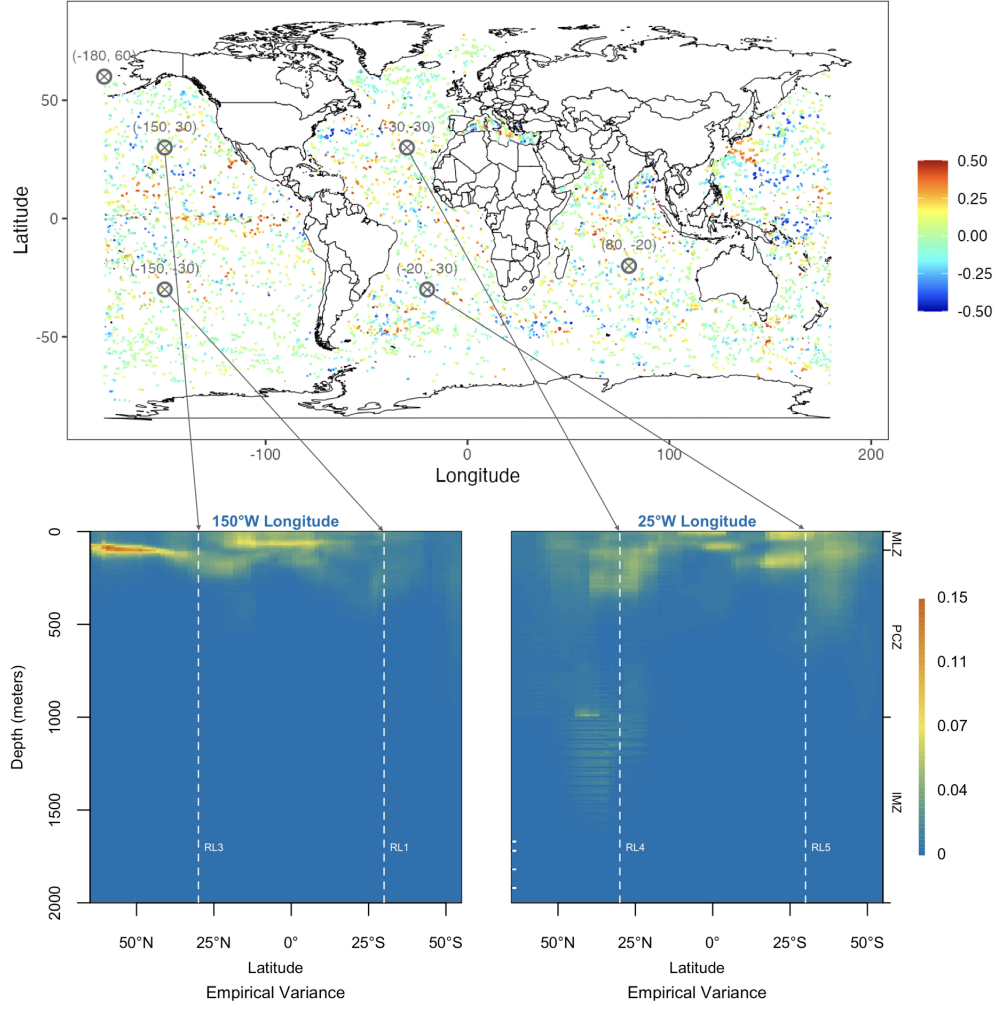


Figure 3: Same as Figure 2 but for salinity residuals.

that values near the equator and along the coasts often differ sharply from their neighbors. This suggests weak spatial dependence in those regions, possibly due to strong localized dynamics or boundary effects. In contrast, over the open ocean, residuals tend to vary more smoothly, with broad contiguous regions (e.g., green areas) exhibiting similar values across space. This indicates stronger spatial dependence in those regions. Apart from these features, no other prominent surface patterns are evident.

More complex patterns emerge below the surface. Suppose $\tilde{\mathcal{D}}$ denotes the volume surrounding a location \mathbf{s} . Using the following formulas:

$$\hat{\sigma}_X^2(\mathbf{s}) = \frac{\sum_{\tilde{\mathbf{s}} \in \tilde{\mathcal{D}}} \{X(\tilde{\mathbf{s}}) - \bar{\mu}_X(\mathbf{s})\}^2}{|\tilde{\mathcal{D}}|} \quad \text{and} \quad \hat{\rho}_{TS}(\mathbf{s}) = \frac{\sum_{\tilde{\mathbf{s}} \in \tilde{\mathcal{D}}} \{T(\tilde{\mathbf{s}}) - \bar{\mu}_T(\mathbf{s})\} \{S(\tilde{\mathbf{s}}) - \bar{\mu}_S(\mathbf{s})\} / |\tilde{\mathcal{D}}|}{\hat{\sigma}_T(\mathbf{s}) \hat{\sigma}_S(\mathbf{s})},$$

we compute the empirical variances and colocated correlation between temperature and salinity, respectively, at each location along the $150^\circ W$ and $25^\circ W$ longitude lines at a $1^\circ \times 1^\circ \times 10$ -meter horizontal and vertical resolution. Here, $\hat{\sigma}_X^2(\mathbf{s})$ is the empirical variance of variable X at \mathbf{s} , where $X = \{T, S\}$ for temperature and salinity, respectively, $\hat{\rho}_{TS}(\mathbf{s})$ is the correlation between temperature and salinity measured at \mathbf{s} . The empirical mean is given by $\bar{\mu}_X(\mathbf{s}) = \sum_{\tilde{\mathbf{s}} \in \tilde{\mathcal{D}}} X(\tilde{\mathbf{s}})/|\tilde{\mathcal{D}}|$. These calculations require measurements of X at locations $\tilde{\mathbf{s}} \in \tilde{\mathcal{D}}$, where $\tilde{\mathcal{D}}$ contains $|\tilde{\mathcal{D}}|$ total locations. In this work, $\tilde{\mathcal{D}}$ is chosen to be a vertical cylinder centered at \mathbf{s} , with a radius of 900 km and a depth of 10 meters. The bottom panels of Figures 2 and 3 display the empirical variances as heatmaps. In addition, Figure 4 shows the heatmap of the empirical colocated correlations.

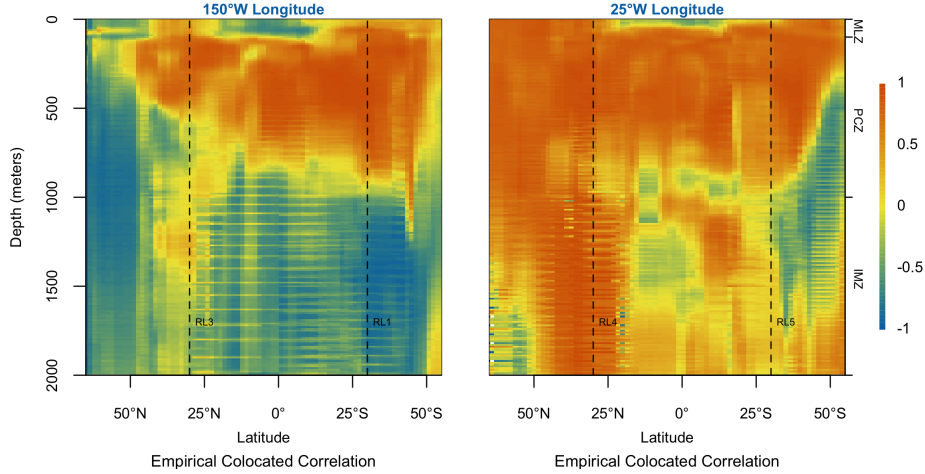


Figure 4: Empirical colocated correlation of temperature and salinity residuals from January to March in 2016.

The empirical variance patterns in Figures 2 and 3 reveal a clear dependence of variance structure on depth. In general, residual variability is higher near the surface and decreases with increasing depth. Notably, there are specific depths—around 200 to 300 meters—where empirical variances drop sharply. These same depths also correspond to where maximum variances are often observed. Such patterns are consistent with prior findings in the literature (McPhaden and Hayes, 1991; Chen and Wang, 2016; Chen et al., 2018; Al Senafi and Anis, 2020; Xie et al., 2000). These observations align with the ocean’s principal horizontal stratification zones based on density, as previously defined, MLZ, PCZ, and IMZ. The MLZ is the uppermost part of

the ocean, typically extending to a depth of about 100 meters, and is directly heated by solar radiation. It is characterized by wind-driven turbulence, waves, and currents, which mix the layer and homogenize temperature and salinity. As a result, this zone often exhibits relatively low vertical variance in the residuals (Helber et al., 2012; Maes and O’Kane, 2014). Below the MLZ lies the PCZ, where water density changes rapidly with depth. This region acts as an invisible barrier separating the warmer, lighter surface waters from the colder, denser deep waters. It typically overlaps with the thermocline (a region of rapid temperature decrease) and the halocline (a region of rapid salinity increase). The PCZ is marked by the highest residual variances, as seen in both temperature and salinity plots. This is likely due to the presence of trapped mesoscale eddies and other submesoscale features that introduce localized, chaotic structures (Dong et al., 2014; Chen and Wang, 2016; Chen et al., 2018). Beneath the PCZ lies the IMZ, a deep, stable layer largely isolated from atmospheric influences. In this region, both temperature and salinity tend to be vertically uniform, which explains the sustained low variances observed below the PCZ boundary.

Figure 4 provides insights on how temperature and salinity interact throughout the water column. Generally, temperature decreases with pressure, while salinity increases. However, this inverse relationship does not always translate directly to the observed correlations between the two variables. From the plot, it can be seen that in a thin surface layer, temperature and salinity are largely uncorrelated, with correlation values near zero. As depth increases and the water column approaches the PCZ, the two variables become strongly positively correlated, with peak correlations observed between approximately 200 and 500 meters. Beyond the PCZ, the colocated cross-correlation displays different pattern along different longitudes. Along the $150^{\circ}W$ longitude line, the correlation decreases again with depth, eventually becoming strongly negative in the IMZ. This vertical transition from independence to strong positive and then negative correlation aligns with findings in Chen and Geng (2019), who describe this behavior as characteristic of the so-called “mirror layer”. In this region, climatological patterns of temperature and salinity

exhibit near-perfect vertical alignment, reinforcing the observed mirror-like behavior. In contrast, this mirror pattern is not evident along the $30^\circ W$ longitude. Instead, high positive correlations persist from the surface down to 2,000 meters. This sustained correlation is consistent with the effects of the meridional overturning circulation (MOC), a major dynamic process in the Atlantic Ocean that transports warm and saline surface waters poleward and returns cooler, fresher water at depth. The mechanism of density compensation—where opposing temperature and salinity anomalies result in a stable density—supports the persistence of the temperature–salinity relationship in this region.

3 Methodology

We have shown that the variances and colocated correlations of the residuals vary with depth, and that the vertical structure at one horizontal location may not be representative of others. To account for such spatial heterogeneity, nonstationary cross-covariance functions defined in the 3D space are needed to provide the vertical expressiveness capable of capturing the depth-dependent variances and colocated correlations observed in the Argo residuals.

3.1 Multivariate Nonstationary Spatial Models in 3D Domain

We treat the temperature and salinity residuals as two distinct zero-mean 3D processes (latitude \times longitude \times depth). Their spatial dependence structure is encoded in a spatial nonstationary cross-covariance function, denoted by $C_{ij}(\mathbf{s}_1, \mathbf{s}_2)$, where $C_{ij}(\mathbf{s}_1, \mathbf{s}_2) = \text{cov} \{Z_i(\mathbf{s}_1), Z_j(\mathbf{s}_2)\}$, $i, j = 1, 2$, such that $Z_1 = T$ and $Z_2 = S$. Here, $Z_i(\mathbf{s}_1)$ represents the value of variable i at location \mathbf{s}_1 , and $Z_j(\mathbf{s}_2)$ represents the value of variable j at location \mathbf{s}_2 , for \mathbf{s}_1 and \mathbf{s}_2 in 3-dimensional space. Only functions that satisfy the well-known condition of positive definiteness can be considered valid models for C_{ij} .

The literature offers a wide array of cross-covariance function models (in 2D space). Among them, the parsimonious Matérn cross-covariance function proposed by Gneiting et al. (2010) is

one among commonly used functions and serves as the foundation for more sophisticated models, which has the form:

$$C_{ij}(\mathbf{s}_1, \mathbf{s}_2) = \frac{\rho_{ij}\sigma_i\sigma_j}{2^{\nu_{ij}-1}\Gamma(\nu_{ij})} \mathcal{M}_{\nu_{ij}}\{h(\mathbf{s}_1, \mathbf{s}_2)\}, \quad (5)$$

for $i, j = 1, \dots, q$, where $h(\mathbf{s}_1, \mathbf{s}_2)$ is a distance function evaluated at locations \mathbf{s}_1 and \mathbf{s}_2 , $\mathcal{M}_\nu(x) = x^\nu \mathcal{K}_\nu(x)$, $\mathcal{K}_\nu(\cdot)$ is the modified Bessel function of the second kind of order ν , $\Gamma(\cdot)$ is the gamma function, and q is the number of variables, which, in our case, $q = 2$. The model includes, for $i = j$, the marginal variance ($\sigma_i^2 > 0$) and smoothness ($\nu_{ii} > 0$) parameters; and for $i \neq j$, the colocated correlation (ρ_{ij}) and cross smoothness ($\nu_{ij} > 0$) parameters, with $\nu_{ij} = \frac{1}{2}(\nu_{ii} + \nu_{jj})$ and

$$\rho_{ij} = \beta_{ij} \frac{\Gamma(\nu_{ii} + \frac{d}{2})^{1/2}}{\Gamma(\nu_{ii})^{1/2}} \frac{\Gamma(\nu_{jj} + \frac{d}{2})^{1/2}}{\Gamma(\nu_{jj})^{1/2}} \frac{\Gamma(\nu_{ij})}{\Gamma(\nu_{ij} + \frac{d}{2})}, \quad (6)$$

for any $\sigma_i^2, \nu_{ii} > 0$, $d \geq 1$. Here, $(\beta_{ij})_{i,j=1}^q$ is a symmetric and positive definite correlation matrix. For 3D spatial processes, we use the following distance function:

$$h(L_1, L_2, l_1 - l_2, p_1 - p_2) = a_h^2 \text{ch}^2(L_1, L_2, l_1 - l_2) + a_v^2 (p_1 - p_2)^2, \quad (7)$$

where a_h and a_v are scale parameters for the horizontal and vertical directions, respectively. The distance function combines horizontal separation, measured using a chordal distance $\text{ch}(L_1, L_2, l_1 - l_2)$ between latitude–longitude pairs, and vertical separation, measured as the Euclidean distance in depth. The chordal distance is defined by:

$$\text{ch}(L_1, L_2, l_1 - l_2) = 2R \left\{ \sin^2 \left(\frac{L_1 - L_2}{2} \right) + \cos L_1 \cos L_2 \sin^2 \left(\frac{l_1 - l_2}{2} \right) \right\}^{1/2}, \quad (8)$$

where R is a constant representing the Earth's radius, taken as 6371 km. While this formulation accommodates the curvature of the Earth, we do not model global covariance structure. Instead, we focus on locally stationary processes in the horizontal directions and allow for nonstationarity along the vertical axis. For completeness, we note that chordal distances are often used to extend valid covariance functions from flat to spherical domains (Jun and Stein, 2007). Further developments for spherical settings can be found in Alegría (2020) and Cao et al. (2024). See

Jeong et al. (2017) on a thorough review and discussion on covariance models on the surface of spheres.

The Matérn cross-covariance function in (5) is stationary and isotropic. Thus, the variances σ_i^2 , the colocated correlations ρ_{ij} , and the scale parameters a_h and a_v are assumed to be constant throughout space. To relax this assumption, Kleiber and Nychka (2012) proposed a nonstationary extension of the parsimonious Matérn cross-covariance model, allowing the variances and scale matrices to vary spatially:

$$C_{ij}(\mathbf{s}_1, \mathbf{s}_2) = \rho_{ij} \sigma_i(\mathbf{s}_1) \sigma_j(\mathbf{s}_2) \mathcal{M}_{\nu_{ij}} \left\{ (\mathbf{s}_1 - \mathbf{s}_2)^\top \mathbf{D}_{ij}(\mathbf{s}_1, \mathbf{s}_2)^{-1} (\mathbf{s}_1 - \mathbf{s}_2) \right\}, \quad (9)$$

where $\mathbf{D}_{ij}(\mathbf{s}) = \frac{1}{2} \{ \mathbf{D}_i(\mathbf{s}_1) + \mathbf{D}_j(\mathbf{s}_2) \}$ is a $d \times d$ positive definite kernel matrix that controls spatially varying anisotropy, for $i, j = 1, \dots, q$. Despite this innovation, a valid extension of the Matérn cross-covariance model that incorporates a nonstationary colocated correlation $\rho_{ij}(\mathbf{s})$ remains elusive. One proposed method is to replace the constants, σ_i^2 and β_{ij} , with kernel-smoothed nonparametric estimators, $\hat{\sigma}_i^2(\mathbf{s})$ and $\hat{\beta}_{ij}(\mathbf{s}_1, \mathbf{s}_2)$, respectively, as suggested by Kleiber and Nychka (2012):

$$\begin{aligned} \hat{\sigma}_i^2(\mathbf{s}) &= \frac{\sum_{\tilde{\mathbf{s}} \in \tilde{\mathcal{D}}} K_{\lambda_h, \lambda_v}(\mathbf{s}, \tilde{\mathbf{s}}) Z_i^2(\tilde{\mathbf{s}})}{\sum_{\tilde{\mathbf{s}} \in \tilde{\mathcal{D}}} K_{\lambda_h, \lambda_v}(\mathbf{s}, \tilde{\mathbf{s}})} \quad \text{and} \\ \hat{\beta}_{ij}(\mathbf{s}_1, \mathbf{s}_2) &= \frac{\sum_{\tilde{\mathbf{s}} \in \tilde{\mathcal{D}}} K_{\lambda_h, \lambda_v}(\mathbf{s}_1, \tilde{\mathbf{s}})^{1/2} K_{\lambda_h, \lambda_v}(\mathbf{s}_2, \tilde{\mathbf{s}})^{1/2} Z_i(\tilde{\mathbf{s}}) Z_j(\tilde{\mathbf{s}})}{\hat{\sigma}_i(\mathbf{s}_1) \hat{\sigma}_j(\mathbf{s}_2) \left\{ \sum_{\tilde{\mathbf{s}} \in \tilde{\mathcal{D}}} K_{\lambda_h, \lambda_v}(\mathbf{s}_1, \tilde{\mathbf{s}}) \right\}^{1/2} \left\{ \sum_{\tilde{\mathbf{s}} \in \tilde{\mathcal{D}}} K_{\lambda_h, \lambda_v}(\mathbf{s}_2, \tilde{\mathbf{s}}) \right\}^{1/2}}, \end{aligned} \quad (10)$$

where $K_{\lambda_h, \lambda_v}(\mathbf{s}, \tilde{\mathbf{s}}) = \exp[-\{\text{ch}^2(L_1, L_2, l_1 - l_2)/\lambda_h + (p_1 - p_2)^2/\lambda_v\}]$ is a nonnegative kernel function with horizontal and vertical bandwidths λ_h and λ_v , respectively, for $i, j = 1, \dots, q$. This approach, however, does not guarantee that the resulting cross-covariance matrix is positive definite. This issue can be remedied by finding the closest positive definite cross-covariance matrix which is done by setting the negative eigenvalues to a very small positive number. Kleiber and Genton (2013) provided parametric forms of $\beta_{ij}(\mathbf{s}_1, \mathbf{s}_2)$ catering to a specific phenomenon involving minimum and maximum temperature residuals over Colorado, which exhibit positive correlation at low elevations and near independence at high elevations. Their method relies on

a nugget effect and is not directly applicable to the bivariate Argo dataset, as the empirical colocated correlations shown in Figure 4 are not monotonic.

A class of spatial nonstationary cross-covariance functions in 2D using differential operators with respect to latitude and longitude was developed in Jun (2011). The univariate version (in space-time setting) was first developed in Jun and Stein (2007). In Jun (2011), the multivariate spatial process can be written in the form:

$$Z_i(L, l) = \sum_{k=1}^K \left\{ a_{i,k}(L) \frac{\partial}{\partial L} + b_{i,k}(L) \frac{\partial}{\partial l} \right\} X_k(L, l) + d_i(L) X_0(L, l), \quad (11)$$

where $X_k(L, l)$, $k = 0 \dots, K$, are independent zero-mean univariate spatial processes, and $a_{i,k}(L)$, $b_{i,k}(L)$, and $d_i(L)$ are non-random functions of the latitude, for $i, j = 1, \dots, q$. The cross-covariance function, i.e., $\text{cov}\{Z_i(L_1, l_1), Z_j(L_2, l_2)\}$ may or may not have a closed form, depending on the univariate spatial covariance function of $X_k(L, l)$. The model in (11) is flexible enough to accommodate negative covariances and allows for spatially varying colocated correlations.

A restriction inherent in the model is that the variables Z_i , for $i = 1, \dots, q$, all rely on the same $X_k(L, l)$, for any k . The model can be made more flexible by replacing the latent univariate spatial processes $X_k(L, l)$ with multivariate spatial processes $\mathbf{X}_k(L, l) = \{X_{1,k}(L, l), \dots, X_{q,k}(L, l)\}^\top \in \mathbb{R}^q$, such that the Z_i 's depend on correlated but distinct underlying components. This modification allows each marginal process Z_i to have its own driving structure while still capturing inter-variable dependence through cross-correlated latent fields. In the following proposition, we propose an extension of (11) with this new innovation and an additional differential operator with respect to depth:

Proposition 1 *Suppose $\mathbf{X}_k(L, l, p)$, $k = 0 \dots, K$, are independent zero-mean multivariate isotropic spatial processes, such that each $\mathbf{X}_k(L, l, p)$ has q elements with cross-covariance function C_{ij}^0 . Let $(L, l, p)^\top$ denote the spatial location in latitude, longitude, and depth. Define a*

multivariate process as follows:

$$Z_i(L, l, p) = \sum_{k=1}^K \left\{ a_{i,k}(L) \frac{\partial}{\partial L} + b_{i,k}(L) \frac{\partial}{\partial l} + c_{i,k}(L, p) \frac{\partial}{\partial p} \right\} X_{i,k}(L, l, p) + d_i(L) X_{i,0}(L, l, p). \quad (12)$$

Furthermore, suppose the cross-covariance function C_{ij}^0 is chosen to be the parsimonious Matérn cross-covariance function in (5). Then, the multivariate process $\mathbf{Z} = (Z_1, Z_2, \dots, Z_q)^\top$ has a matrix-valued nonstationary cross-covariance function given by:

$$C_{ij}(L_1, L_2, l_1 - l_2, p_1, p_2) = K_{ij}^1 \mathcal{M}_{\nu_{ij}-1} \{h(L_1, L_2, l_1 - l_2, p_1 - p_2)^{1/2}\} \\ + K_{ij}^2 \mathcal{M}_{\nu_{ij}} \{h(L_1, L_2, l_1 - l_2, p_1 - p_2)^{1/2}\}, \quad (13)$$

where

$$K_{ij}^1 = \frac{\alpha_{ij}}{4} \sum_{k=1}^K \{ a_{i,k}(L_1) a_{j,k}(L_2) h_1 h_2 - b_{i,k}(L_1) b_{j,k}(L_2) h_3^2 - c_{i,k}(L_1, p_1) c_{j,k}(L_2, p_2) h_4^2 \\ - a_{i,k}(L_1) b_{j,k}(L_2) h_1 h_3 + a_{j,k}(L_2) b_{i,k}(L_1) h_2 h_3 - a_{i,k}(L_1) c_{j,k}(L_2, p_2) h_1 h_4 \\ + a_{j,k}(L_2) c_{i,k}(L_1, p_1) h_2 h_4 - b_{i,k}(L_1) c_{j,k}(L_2, p_2) h_3 h_4 - b_{j,k}(L_2) c_{i,k}(L_1, p_1) h_3 h_4 \} \\ + \alpha_{ij} h d_i(L_1) d_j(L_2), \\ K_{ij}^2 = -\frac{\alpha_{ij}}{2} \sum_{k=1}^K \{ a_{i,k}(L_1) a_{j,k}(L_2) h_{12} - b_{i,k}(L_1) b_{j,k}(L_2) h_{33} - c_{i,k}(L_1, p_1) c_{j,k}(L_2, p_2) h_{44} \\ - a_{i,k}(L_1) b_{j,k}(L_2) h_{13} + a_{j,k}(L_2) b_{i,k}(L_1) h_{23} \} + 2\alpha_{ij} \nu_{ij} d_i(L_1) d_j(L_2),$$

$$\text{and } \alpha_{ij} = \frac{\rho_{ij} \sigma_i \sigma_j}{2^{\nu_{ij}-1} \Gamma(\nu_{ij})}.$$

The proof of the proposition is rather straightforward. Refer to Appendix in Jun and Stein (2007) for the exact expressions of h_r and h_{rs} , for $r, s = 1, \dots, 4$.

The formulation in Proposition 1 represents a substantial generalization of the earlier model in (11). While the original model is defined over 2D (spherical) spatial domains (latitude and longitude), Proposition 1 extends the construction to 3D space by explicitly incorporating depth as an additional spatial coordinate. This extension enables the modeling of spatial dependence

structures that evolve with depth, a key feature in oceanographic applications where vertical stratification plays a dominant role.

Another major advancement is the structural flexibility introduced through a richer latent process structure. In the original model, all components Z_i share the exact same set of latent processes $X_k(L, l)$ and $X_0(L, l)$, resulting in colocated correlations of one across all variables, i.e., $\rho_{ij} = 1$ for any $i \neq j$. This is because the randomness in all Z_i and Z_j arises from identical underlying sources. By contrast, Proposition 1 allows each variable Z_i to be driven by its own latent process $X_{i,k}(L, l, p)$, which can differ across i , even for the same index k . The dependence between variables is then introduced through the cross-covariance of these latent fields, with colocated correlation ρ_{ij} defined specifically as the correlation between $X_{i,k}(L, l, p)$ and $X_{j,k}(L, l, p)$. This formulation relaxes the rigid assumption of perfect inter-variable dependence and allows the colocated correlation ρ_{ij} to be less than one, enabling the model to capture more realistic relationships between physical variables such as temperature and salinity.

The differential operator framework in Proposition 1 is designed to accommodate spatial nonstationarity in both latitude and depth, reflecting the known influence of these dimensions on large-scale geophysical processes. In particular, the inclusion of a vertical derivative term $\partial/\partial p$ with a spatially varying coefficient $c_{i,k}(L, p)$ allows the model to flexibly capture changes in covariance structure across depth—a crucial feature in oceanographic settings where stratification and thermocline dynamics dominate vertical variability. While the general formulation permits latitude-dependent coefficients—such as $a_{i,k}(L)$, $b_{i,k}(L)$, and $c_{i,k}(L, p)$ —our implementation focuses on vertical nonstationarity within localized regions. Specifically, we fit the model separately at each of six reference locations. Within each location, we treat the coefficients $a_{i,k}$ and $b_{i,k}$ as constants, assuming local stationarity in the horizontal (latitude–longitude) plane. Vertical nonstationarity is introduced through the coefficient $c_{i,k}(p)$, which is allowed to vary with depth to reflect depth-dependent behavior. This modeling strategy leverages the full generality of the framework while directing flexibility to the vertical axis, where ocean processes

exhibit the strongest and most systematic heterogeneity.

3.2 Modeling vertical coefficients for differential operators

We now present our strategies in modeling $c_{i,k}(p)$ in a parsimonious and interpretable way. There is no restriction or condition on $c_{i,k}(p)$ to guarantee the positive definiteness of the covariance models. In earlier work on 2D spatial domains, Jun and Stein (2008) and Jun (2011) introduced nonstationarity in latitude by expressing the coefficients $a_{i,k}(L)$ and $b_{i,k}(L)$ using spherical harmonics. Inspired by this idea, we generalize the approach to 3D space and represent the vertical coefficient $c_{i,k}(p)$ using basis functions in depth.

We discuss a few choices of the basis functions to represent the coefficients of the differential operators to achieve vertical nonstationarity. Basis function expansions play a central role in ensuring that the resulting covariance model can flexibly accommodate spatial variation in the vertical dimension. For a fixed latent index k , the function $c_{i,k}(p)$, which governs the strength of the vertical derivative operator, is written as:

$$c_{i,k}(p) = \sum_{m=0}^{M_i} \eta_{i,m}^{(k)} B_{i,m}(p), \quad (14)$$

where $\eta_{i,m}^{(k)}$ are the expansion coefficients and $B_{i,m}(p)$ are basis functions defined over the normalized depth domain $p \in [0, 1]$.

Following the construction in Jun and Stein (2008) and Jun (2011), we consider Legendre polynomials as a natural choice for $B_{i,m}$. If $P_m(x)$ denotes the m th Legendre polynomial defined on $x \in [-1, 1]$, we define $B_{i,m}(p) = P_m(2p - 1)$ after rescaling the depth variable p to the unit interval. This orthogonal polynomial basis provides smooth global representations for vertical dependence and is well-suited for modeling layered ocean structure.

An alternative to orthogonal polynomials is the use of B-spline basis functions to represent $c_{i,k}(p)$. B-splines are piecewise polynomial functions that achieve flexibility by joining polynomial segments at predefined knot locations, allowing localized control over the shape of the coefficient

function (Kunoth et al., 2018). Let $\mathcal{B}_m(p)$ denote the m th B-spline basis function of a chosen order. Then the basis expansion is written as $B_{i,m}(p) = \mathcal{B}_m(p)$. The placement and spacing of knots can be tailored to the variable of interest or the structure of the data, with closely spaced knots enabling finer resolution to capture sharp vertical transitions. However, using a large number of knots increases the number of parameters and can complicate estimation due to potential convergence issues.

Both Legendre polynomials and B-splines are capable of producing flexible nonstationary covariance structures along the vertical depth axis. For our application, we found that Legendre polynomial bases provided a better overall fit when comparing models with an equal number of parameters (i.e., same polynomial order versus number of spline knots). This basis will therefore be used in the subsequent modeling.

To understand how $c_{i,k}(p)$ and $c_{j,k}(p)$ affect model behavior, we examine their role in shaping the vertical structure of dependence. These functions directly influence the marginal variance, $C_{ii}(L, L, 0, p, p)$, and the cross-covariance, $C_{ij}(L, L, 0, p, p)$, thereby controlling how spatial variability and inter-variable dependence evolve with depth. This is particularly important for capturing the layered nature of the ocean, where the surface mixed layer, the pycnocline, and the deeper stratified zones exhibit distinct covariance behavior. The vertical modulation encoded by $c_{i,k}(p)$ thus enables the model to reflect realistic, location-specific heterogeneity across depth levels. To illustrate this, we consider the behavior of the colocated correlation curve

$$\frac{C_{ij}(L, L, 0, p, p)}{\sqrt{C_{ii}(L, L, 0, p, p)C_{jj}(L, L, 0, p, p)}},$$

under a model with $q = 2$ variables and $d_1 = d_2 = 0$. For simplicity and model parsimony, we set $K = 1$ throughout this work, following the approach in Jun and Stein (2007) and Jun and Stein (2008). Accordingly, we drop the latent process index k from the notation and refer to the coefficients as a_i , b_i , and $c_i(p)$, where $c_i(p)$ governs the vertical structure of variable i .

The functions $c_1(p)$ and $c_2(p)$ used in this illustration were constructed from degree-5 Legendre

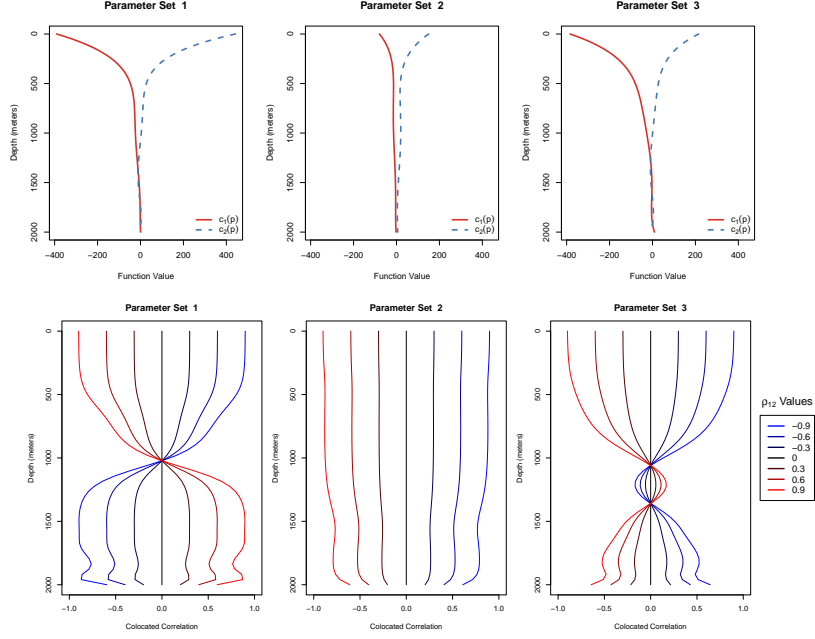


Figure 5: Vertical shape of $c_i(p)$ as a function of depth (p) for three different set of coefficients for c_i 's (top row) and resulting collocated correlation curves (bottom row). Collocated correlation curves are varied with varying $\rho_{12} = -0.9, \dots, 0.9$.

polynomials and estimated from real temperature and salinity residual data at three reference locations as in Section 4: RL1, RL4, and RL5. These correspond to three distinct sets of vertical structures. Top panel of Figure 5 displays these estimated coefficient functions. In each panel, the red solid curve denotes $c_1(p)$, and the blue dashed curve denotes $c_2(p)$, with depth increasing from the surface (0 meters) to 2,000 meters. The distinct patterns observed across the three panels highlight the model's ability to encode heterogeneous vertical structures across spatial regions. Using these estimated functions, the bottom panel of Figure 5 shows the resulting collocated correlation curves as a function of depth, for a range of values of the inter-variable coupling parameter $\rho_{12} \in (-1, 1)$. These curves illustrate how the shape of vertical dependence is modulated by $c_1(p)$ and $c_2(p)$, while ρ_{12} controls the amplitude of the correlation. This construction allows the model to separate structural modulation from interaction strength.

3.3 Likelihood approximation

For the estimation of parameters, we use the maximum likelihood estimation (MLE) to jointly estimate all parameters. Despite employing a local stationary framework, the size of the Argo residuals dataset renders the matrix operations needed in the likelihood computation infeasible. Specifically, the Gaussian likelihood requires the inversion of the covariance matrix that has a $\mathcal{O}(N^2q^2)$ memory complexity and a $\mathcal{O}(N^3q^3)$ computation complexity, where N is the number of spatial locations.

Many methods have been proposed in the literature to approximate Gaussian likelihoods; see Heaton et al. (2019) and Liu et al. (2020b) for a comprehensive review of such approaches for spatial data. Among these, we adopt the Vecchia approximation (Vecchia, 1988). The Vecchia approximation is typically applied to univariate Gaussian processes (i.e., $q = 1$) and is based on truncating the conditioning in the joint density decomposition:

$$f(\mathbf{x}) = \prod_{w=1}^N f(x_w | \mathbf{x}_{1:w-1}) \approx \prod_{w=1}^N f(x_w | \mathbf{x}_{\tau(w)}), \quad (15)$$

where \mathbf{x} is a random vector of length N , $f(\cdot)$ is a generic density function, and $\tau(w)$ is the conditioning set of x_w , commonly chosen as the u nearest neighbors of x_w among $\{x_1, \dots, x_{w-1}\}$ (Katzfuss and Guinness, 2021). The parameter u serves as a tuning parameter that balances the computation cost with the bias introduced by the approximation and is usually set such that $u \ll N$ (e.g., $u = 30$ for $N = 5,000$). Finding nearest neighbors requires a distance function defined over the domain of the response variables, for which we use \sqrt{h} with h defined in (7) and computed at $a_h = a_v = 1$. The conditioning sets $\{\tau(w)\}$ may vary with a_h and a_v but its impact on parameter estimation is usually insignificant and any choice of $\{\tau(w)\}$ leads to unbiased estimators (Cao et al., 2022). In our implementation, we fix $\{\tau(w)\}$ during optimization to enable automatic differentiation and improve computation efficiency but note that Katzfuss and Guinness (2021) proposes to re-calculate the conditioning sets $\{\tau(w)\}$ after a number of iterations during optimization. For multivariate Gaussian processes, we substitute the

random variable x_w with a random vector of length q , for example, $[z_1(\mathbf{s}_w), z_2(\mathbf{s}_w), \dots, z_q(\mathbf{s}_w)]^\top$, representing the q variables observed at the w -th spatial location, under which the complexity for likelihood estimation becomes $\mathcal{O}(Nu^3q^3)$.

4 Application

We now fit the covariance models developed to the joint modeling of temperature and salinity variables from Argo floats and compare with the classic parsimonious Matern model. The results demonstrate the utility of the proposed approach in capturing the vertical structure of the data as well as the non-stationary cross-correlation between the two variables.

4.1 Data

Due to the sheer size of the full Argo dataset and the horizontal nonstationarity of ocean variables, modeling is performed one local region—i.e., one reference location—at a time. We consider six reference locations (RLs) selected to align with major patterns of ocean circulation, as highlighted in Section 2. These RLs were strategically chosen to ensure comprehensive spatial representation across diverse oceanic regimes. Marked with circled X symbols on the temperature and salinity residual maps (Figures 2 and 3), the locations span varying latitudes (high: 60° , mid: $\pm 30^\circ$, equatorial: $\pm 20^\circ$) and key longitudinal bands (-180° , -150° , -30° , 30° , 80°) to capture the thermohaline diversity of the global ocean. Each reference location lies within the domain of a major ocean circulation system: RL1 and RL2 monitor the North Pacific Current; RL3 captures dynamics of the South Pacific circulation; RL4 tracks the Gulf Stream and North Atlantic Current; RL5 assesses the Brazil Current; and RL6 examines the East Australian Current. This distribution facilitates a comparative analysis of model performance across contrasting oceanographic environments characterized by different temperature and salinity variability patterns. It also provides key insights into the spatial adaptability of our modeling framework across regions with distinct physical forcing.

Table 1: Counts of available floats and observations per variable, for each reference location.

RL	Training		Testing	
	# floats	# obs	# floats	# obs
1	29	14,913	7	5,051
2	24	15,475	6	3,946
3	79	25,688	20	7,001
4	66	19,747	16	3,938
5	59	24,553	15	7,570
6	64	28,179	16	7,067

We use the 2016 residuals located within a vertical cylinder of radius 900 km centered at each reference location. Table 1 summarizes the number of floats and total measurements available per region. Note that floats vary in the number of vertical measurements collected. In all six locations, some floats span the full depth range of 0 to 2,000 meters, while others cover only up to 1,200 meters. For each reference location, floats are randomly divided into training and testing sets using an 80-20 split.

Before modeling temperature and salinity data as a bivariate Gaussian random field, we assessed the Gaussianity of the temperature and salinity residuals around the six reference locations. Histograms and Q-Q plots indicate that, in most ocean sub-regions, the data do not show significant deviations from the Gaussian assumption (see Figures A.1 and A.2 in the Appendix). Several prior studies have also modeled temperature and salinity as Gaussian processes (Böhme and Send, 2005; Cabanes et al., 2016). In cases where non-Gaussian behavior is observed, common practice in the literature involves preprocessing the data to remove outliers before fitting Gaussian models (Chaigneau et al., 2011). For the six reference locations used in this study, we model the residuals without additional preprocessing, as we did not detect any strong violations of Gaussianity.

4.2 Covariance models

For the bivariate modeling of temperature and salinity residuals, we compare three covariance models:

- M1: bivariate parsimonious Matérn cross-covariance function with constant variances and a constant colocated correlation parameter; see Equation (5);
- M2: independent differential operator with Matérn covariance function; see Equation (13) where $\rho_{12} = 0$;
- M3: bivariate differential operator with bivariate parsimonious Matérn cross-covariance function; see Equation (13).

These models vary in terms of inter-process dependence and vertical nonstationarity. In the descriptions above, “independent” models refer to those that allow distinct marginal structures for temperature and salinity but assume zero cross-correlation between them. Table 2 summarizes the main features and parameter counts for each model.

In a preliminary analysis, we fitted univariate Matérn models to each variable at all six reference locations and found that the estimated smoothness parameters for both temperature and salinity were consistently around 2. Based on this finding, we fixed the smoothness to 2 across all models. To incorporate vertical nonstationarity, as discussed in Section 3.2, the coefficient function $c_i(L, p)$ is modeled as a function of pressure alone, denoted $c_i(p)$, using a basis expansion as in Equation (14) with Legendre polynomials as basis functions. We experimented with various polynomial orders and observed negligible improvements in model fit (e.g., likelihood values) beyond order 5. Accordingly, we used degree-5 Legendre polynomials for both variables (i.e., $M_1 = M_2 = 5$) throughout our analysis. As shown in Table 2, this results in 20 parameters for M2 and 21 parameters for M3.

Table 2: Summary of model properties and number of parameters.

Model	Properties	# Parameters
M1	parametric, stationary, bivariate	5
M2	parametric, nonstationary, independent	20
M3	parametric, nonstationary, bivariate	21

4.3 Fitted results

We now examine the performance of the three candidate spatial covariance models, M1–M3, in modelling the residuals around the six reference locations. Each location exhibits a distinct vertical dependence structure, as evident in Figures 2–4, which some models may capture more effectively than others. We evaluate and compare model performance based on how well each model explains the observed residuals, using both log-likelihood values and the Akaike Information Criterion (AIC) as metrics.

The results are summarized in Table 3. Both the log-likelihood and AIC values demonstrate that the proposed bivariate model M3 consistently outperforms M1 and M2 across all six reference locations. This improvement reflects the enhanced flexibility of M3 in capturing both nonstationary marginal variance and nonzero cross-correlation between temperature and salinity, made possible by the differential operator kernel parameterization. While M2 incorporates vertical nonstationarity through flexible marginal variances, its assumption of zero cross-correlation generally limits its performance relative to M3, although it still outperforms the simpler stationary model M1 in most cases. Notably, the estimated colocated cross-correlation $\hat{\rho}_{12}$ values under M3 are consistently larger than those from M1 (except at RL3), suggesting that M3 better captures inter-variable dependence. In addition, the estimated horizontal and vertical scale parameters under M2 and M3 are broadly consistent with each other, yet they differ substantially from those of M1, which assumes stationarity and lacks flexibility in vertical structure.

Figure 6 displays the fitted colocated correlation curves produced by the three models, overlaid with empirical estimates from the training data (in black) as a function of depth. Depth is divided into bins of 2 meters, and empirical colocated correlations are computed within each bin by pooling all available data. Across all six reference locations, the fitted curves from model M3 align closely with the empirical colocated correlations, successfully capturing the complex vertical dependence structure from the surface down to 2000 meters. While the fit is not perfect at RL2 and RL3, M3 still demonstrates substantially better agreement with the data than the

Table 3: Parameter estimates and performance summaries for M1, M2, and M3 using datasets collected at reference locations 1 through 6. For parameter estimates, values in parentheses indicate asymptotic standard errors. Higher log-likelihood and lower AIC values indicate better model fit. The best values per reference location are shown in **bold**.

Reference Location	Model	$\hat{\rho}_{12}$	horizontal scale, \hat{a}_h	vertical scale, \hat{a}_v	$\hat{\sigma}_1$	$\hat{\sigma}_2$	log-likelihood ($\times 10^3$)	AIC ($\times 10^3$)
RL1	M1	0.723 (4.3e-03)	903 (57.6)	263 (0.79)	0.467 (2.4e-03)	0.457 (2.35e-03)	55.1	-110
	M2	– (1.98)	357 (1.98)	14.2 (0.04)	2.96e-05 (1.18e-07)	5.5e-05 (2.8e-07)	78	-156
	M3	0.895 (4.7e-03)	291 (2.25)	75.3 (0.21)	1.57e-04 (7.93e-07)	2.33e-04 (1.22e-06)	99.6	-199
RL2	M1	0.925 (1.4e-03)	934 (20)	190 (0.66)	0.378 (1.61e-03)	0.361 (1.53e-03)	82.3	-165
	M2	– (3.08)	503 (3.08)	75.5 (0.24)	6.37e-05 (3.62e-07)	1.37e-04 (7.78e-07)	119	-238
	M3	0.953 (1.6e-03)	447 (2.25)	75.9 (0.26)	1.61e-04 (7.85e-07)	2.46e-04 (1.2e-06)	122	-244
RL3	M1	0.891 (1.9e-03)	3005 (326)	167 (0.49)	0.72 (2.72e-03)	0.791 (2.87e-03)	90.8	-182
	M2	– (6.95)	1041 (6.95)	81.6 (0.17)	4.43e-05 (2e-07)	7.44e-05 (3.34e-07)	131	-261
	M3	0.786 (5.1e-03)	1008 (6.13)	84.6 (0.18)	5.36e-05 (2.24e-07)	7.43e-05 (3.1e-07)	133	-266
RL4	M1	0.935 (9e-04)	963 (18)	186 (0.58)	0.607 (2.02e-03)	0.36 (1.2e-03)	84.6	-169
	M2	– (10.5)	1010 (10.5)	89.9 (0.19)	1.62e-04 (8.17e-07)	1.12e-04 (5.68e-07)	86.6	-173
	M3	0.993 (2e-04)	352 (2.81)	62.8 (0.12)	8.19e-04 (2.5e-06)	2.5e-04 (7.63e-07)	97	-194
RL5	M1	0.675 (4.7e-03)	629 (16.2)	175 (0.49)	0.857 (3.63e-03)	0.371 (1.57e-03)	99.5	-199
	M2	– (3.24)	558 (3.24)	75.4 (0.16)	1.01e-04 (4.58e-07)	1.82e-04 (8.23e-07)	152	-304
	M3	0.917 (2.8e-03)	531 (2.78)	79.9 (0.17)	6.12e-05 (2.53e-07)	2.27e-04 (9.42e-07)	155	-310
RL6	M1	0.317 (0.0111)	1962 (76.6)	121 (0.36)	1.6 (6.71e-03)	1.72 (7.19e-03)	72.6	-145
	M2	– (4.89)	613 (4.89)	38.8 (0.07)	1.09e-04 (4.54e-07)	8.26e-05 (3.43e-07)	139	-278
	M3	0.912 (2.2e-03)	633 (3.84)	60 (0.12)	8.5e-05 (3.23e-07)	1.14e-04 (4.33e-07)	144	-289

other models. Model M2, which assumes independence between variables, fails to reflect the strong cross-correlation observed in all six regions. Similarly, the baseline stationary model M1 is unable to reproduce the depth-varying pattern of inter-variable dependence, leading to a poor overall fit. These results highlight the inadequacy of stationary models like M1 for representing realistic vertical dependence and emphasize the utility of flexible, vertically nonstationary models

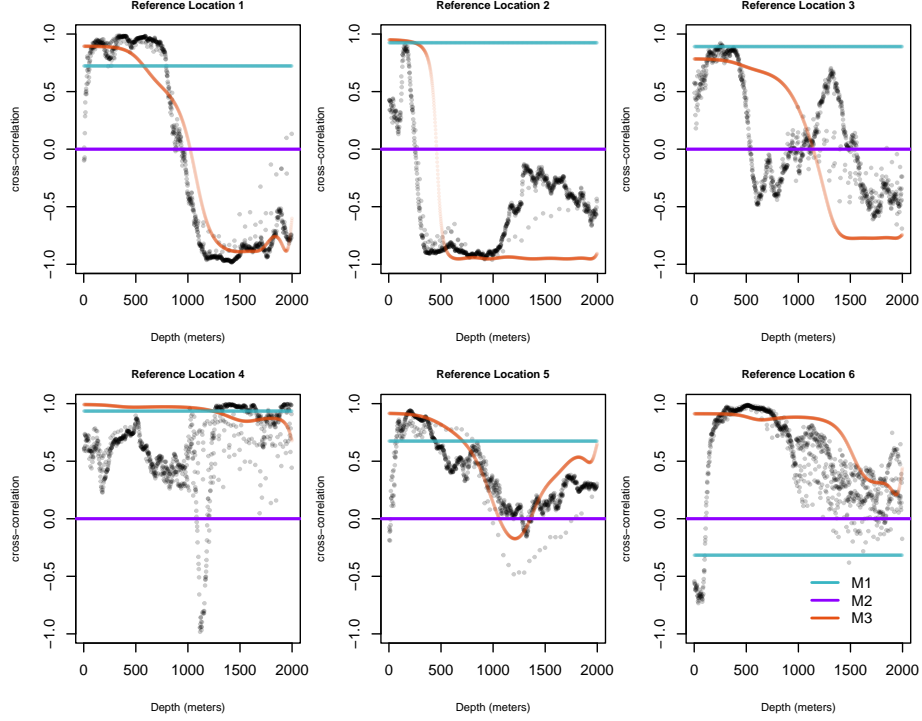


Figure 6: Empirical (black) and model-based estimates of colocated correlations plotted as a function of depth for each reference location. Empirical values are computed as sample cross-correlations of temperature and salinity from all training floats within non-overlapping vertical bins of 2-meter width. Model M1 produces constant correlations across depth; M2 yields zero throughout; M3 tracks the empirical patterns.

such as M3.

4.4 Kriging results

We now assess the performance of the three models by evaluating how well they predict the measurements at testing floats. As shown in Table 1, 20% of floats from each reference location were randomly selected and withheld for testing purposes. Kriging was performed for both temperature and salinity at each testing float, using the values from the five geographically closest training floats.

A central challenge in this task is the pronounced variability in vertical structure across floats, even within localized geographic regions. Figure 7 compares the temperature and salinity residual profiles of testing floats against their nearest training float (in terms of horizontal distance) at two reference locations: RL1 (7 testing floats) and RL2 (6 testing floats). The other 4

reference locations have more floats, and displaying and comparing profiles from each of the floats would be more difficult. Profiles from testing floats are shown in thick solid lines, and the corresponding profiles from the training floats are shown in dotted lines of the same color. The discrepancies between testing and training data are striking for both reference locations and both variables. While in some cases the solid and dotted curves match closely, in many others they diverge significantly—especially within the upper 1,000 meters of the water column. These observations indicate either horizontal nonstationarity or weak horizontal correlation and highlight the difficulty of prediction, even when using covariance models explicitly designed to accommodate nonstationary structure. Notably, some of these discrepancies between nearby floats may stem from the fact that floats are displaced horizontally as they travel vertically. Argo float data report a single longitude–latitude coordinate per profile, although floats may drift laterally due to ocean turbulence and other dynamic factors while profiling (Wang et al., 2020; Merchel et al., 2024).

Nevertheless, we compute the Mean Absolute Error (MAE) of predicted temperature and salinity residuals as a function of ocean depth to evaluate the depth-dependent predictive performance of the models. MAE is calculated separately for each of the six reference locations and for each of the two variables—temperature and salinity—across three model configurations (M1, M2, and M3). Since there are multiple testing floats per reference location, we summarize MAE values by binning ocean depth into 100-meter intervals: $[0,100)$, $[100,200)$, \dots , $[1900,2000]$ meters. Within each bin, we pool the residuals from all Argo testing floats associated with the corresponding reference location. That is, for a given location, variable, and model, we collect all prediction errors from different testing Argo profiles whose observation depths fall within a given bin. This pooling ensures that each depth interval is adequately populated with residuals and allows for robust estimation of the bin-specific MAE. Specifically, let z_w^{true} and z_w^{pred} denote the true and predicted values of either temperature or salinity at depth d_w , and let $\mathcal{D}_b = \{w : d_w \in \text{bin}_b\}$

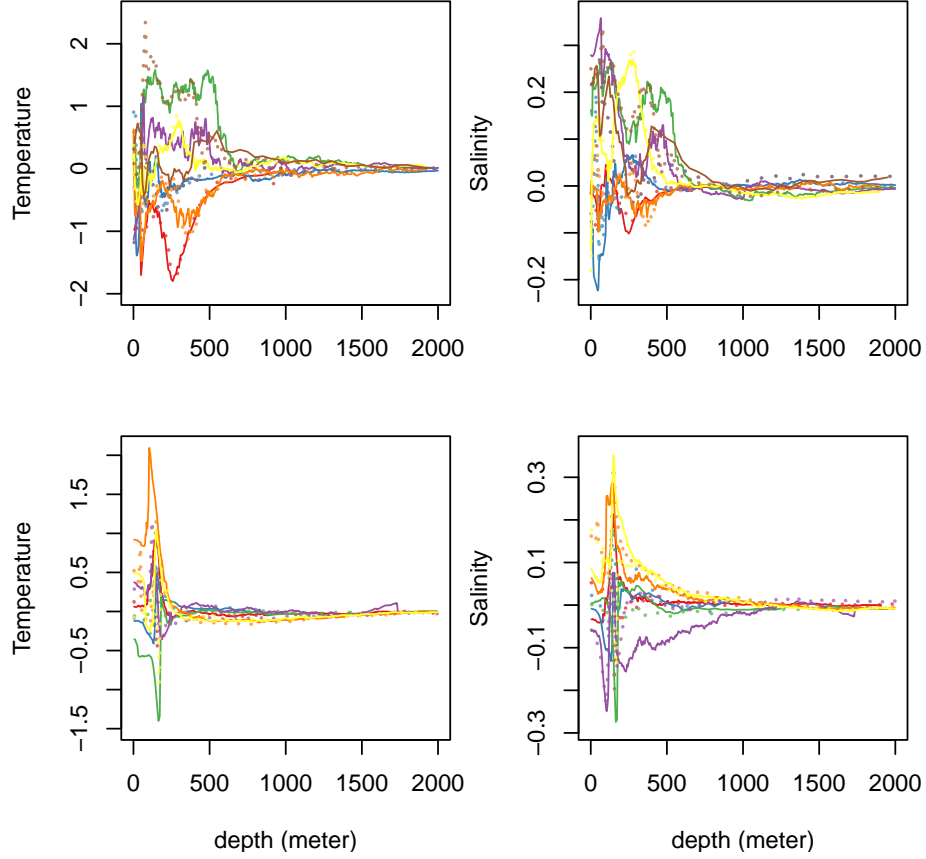


Figure 7: Comparison between residual profiles from testing floats and their (horizontally) nearest training float at reference locations 1 (top row) and 2 (bottom row), for temperature residuals (left) and salinity residuals (right). For each testing float (solid curve), the corresponding training float is displayed in the same color with a dotted line.

denote the set of indices for observations in bin b . The MAE for that bin is then given by:

$$\text{MAE}_b = \frac{1}{|\mathcal{D}_b|} \sum_{w \in \mathcal{D}_b} |z_w^{\text{true}} - z_w^{\text{pred}}|.$$

Figure 8 displays the MAE values as a function of depth for each reference location. In all six locations, we observe a consistent pattern: the highest MAE values occur near the surface (depth 0–500 m), with a sharp decline in error as depth increases. This behavior aligns with the known physical structure of the ocean, where greater temperature and salinity variability—and stronger gradients—are found in the upper layers, particularly within the thermocline. Below 500 m, MAE generally stabilizes, reflecting reduced variability and improved predictive accuracy. Across all six reference locations, M1 produces the highest Kriging errors, with particularly poor performance

at reference location 6. While M2 and M3 have similar predictive performance overall, there is a clear advantage for M3 at reference location 4. This is consistent with the nearly perfect colocated cross-correlation between temperature and salinity at that location. Since M2 ignores cross-variable dependence, its performance degrades significantly in this setting—underperforming both M3 and even M1.

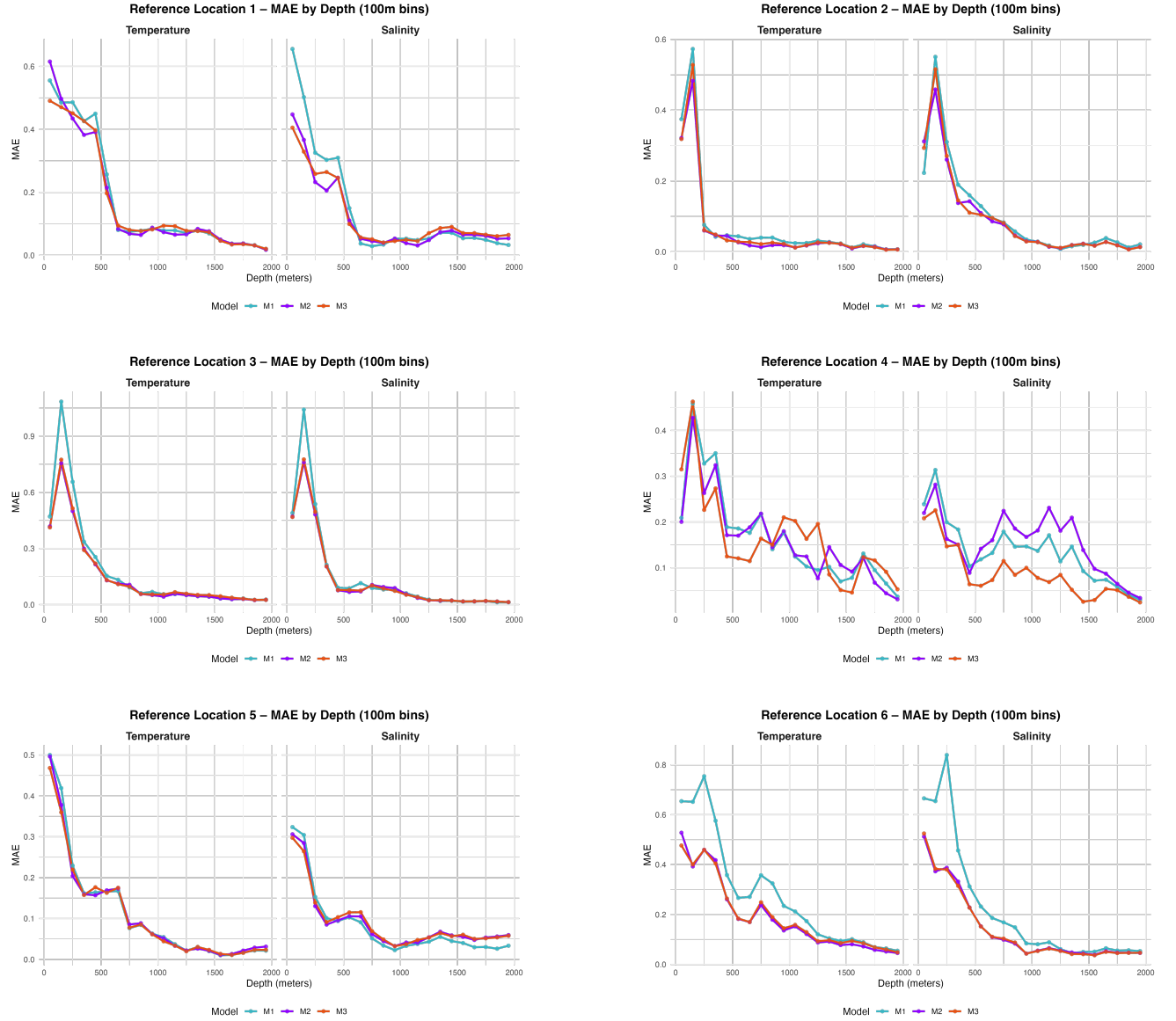


Figure 8: MAE by depth across reference locations 1–6. Each panel shows model performance at predicting temperature and salinity as a function of depth (binned in 100 m intervals).

Figure 9 summarizes the number of available testing observations in each bin, grouped by reference location. Each curve represents the observation count per bin for one location, allowing

a direct comparison of vertical data coverage. This analysis highlights variability in sampling density with depth and reveals location-specific differences in observational coverage. Notably, data coverage tends to decrease with increasing depth, although the rate and pattern of decline vary across sites.

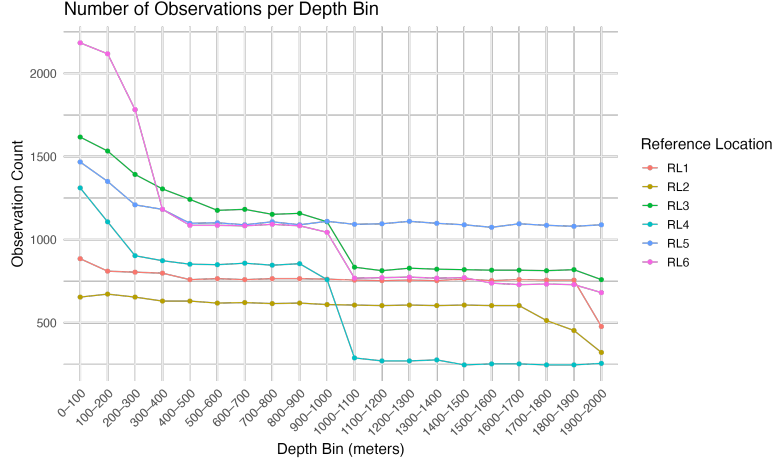


Figure 9: Number of testing observations per 100-meter depth bin for each reference location. The depth bins range from 0 to 2,000 meters, and the x -axis labels indicate bin boundaries.

4.5 Model diagnostics on differenced processes

In order to further diagnose the proposed models' ability to capture spatial variation and correlation structure of the processes, we compare the empirical and fitted covariance structures of differenced processes. Specifically, we consider the first and second differencing of processes along the vertical dimension. That is, for each $Z_i(L, l, p)$, we define its first differenced process:

$$Z_i^{(1)}(L, l, p) = Z_i(L, l, p) - Z_i(L, l, p + \Delta p),$$

and its second differenced process:

$$Z_i^{(2)}(L, l, p) = -Z_i(L, l, p + \Delta p) + 2 Z_i(L, l, p) - Z_i(L, l, p - \Delta p).$$

We set $\Delta p = 2$ meters, and differencing is performed separately for each profile. The corresponding differencing matrices are defined below in Equation (17).

The marginal and cross-covariance structures of the differenced bivariate process $\mathbf{Z}^{(k)} = (Z_1^{(k)}, Z_2^{(k)})^\top$ for $k = 1, 2$, are computed as linear combinations of the base covariances C_{ij} from Equation (13). For instance, under the assumption of axial symmetry (i.e. stationarity in longitude), the first-differenced covariance is given by:

$$\begin{aligned} \text{Cov}\{Z_i^{(1)}(L, l, p), Z_j^{(1)}(L, l, p)\} &= C_{ij}(L, L, 0, p, p) + C_{ij}(L, L, 0, p + \Delta p, p + \Delta p) \\ &\quad - C_{ij}(L, L, 0, p, p + \Delta p) - C_{ij}(L, L, 0, p + \Delta p, p). \end{aligned} \quad (16)$$

To carry out differencing in practice, we apply the following matrices to the data vector of each profile (ordered by increasing depth) for the first differencing (T_1) and second differencing (T_2):

$$T_1 = \begin{pmatrix} 1 & 0 & 0 & 0 & \cdots & 0 \\ -1 & 1 & 0 & 0 & \cdots & 0 \\ 0 & -1 & 1 & 0 & \cdots & 0 \\ & & \ddots & \ddots & & \\ 0 & 0 & \cdots & -1 & 1 & 0 \\ 0 & 0 & \cdots & 0 & -1 & 1 \end{pmatrix} \quad \text{and} \quad T_2 = \begin{pmatrix} 2 & -1 & 0 & 0 & \cdots & 0 \\ -1 & 2 & -1 & 0 & \cdots & 0 \\ 0 & -1 & 2 & -1 & \cdots & 0 \\ & & \ddots & \ddots & \ddots & \\ 0 & 0 & \cdots & -1 & 2 & -1 \\ 0 & 0 & \cdots & 0 & -1 & 2 \end{pmatrix}. \quad (17)$$

If $\Sigma = (\Sigma_{ij})_{i,j=1,2}$ denotes the 2×2 block covariance matrix of temperature and salinity residuals for a given profile, then the covariance matrix of the differenced process is:

$$\Sigma^{(k)} = T_k \Sigma_{ij} T_k^T, \quad (18)$$

for $k = 1$ (first differencing) or $k = 2$ (second differencing).

To obtain empirical covariance values from the Argo data, we apply first or second differencing along the vertical pressure levels for each float. This is justified by the fact that most observations within a single float profile share the same longitude and latitude. Furthermore, between depths of 0 and approximately 1,200 meters, the pressure levels are typically sampled at 2-meter intervals, while sampling becomes sparser below 1,200 meters. For each level p_m , we calculate the difference between temperature (or salinity) residuals at the level p_m and the

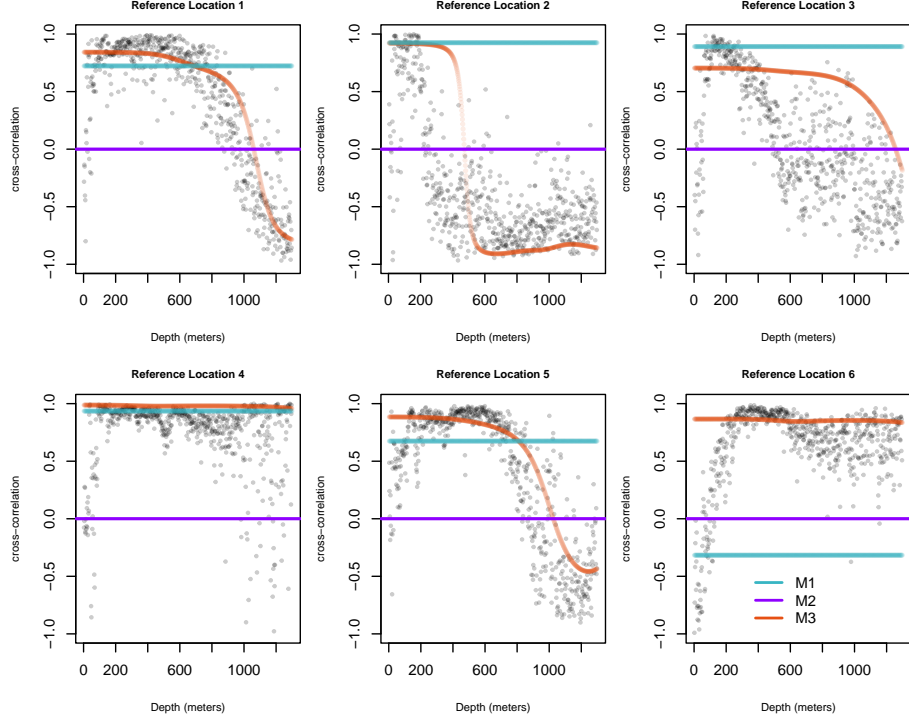


Figure 10: Empirical (black) and model-based estimates of colocated correlations of the first differenced processes, plotted as a function of depth at each reference location.

adjacent pressure levels, $p_m + \Delta p$ and $p_m - \Delta p$ for each float with $\Delta p = 2$ meters, except the very top and very bottom level, where differencing follows the scheme in Equation (17). Empirical variances and covariances are then computed using the differenced values from all floats within the local region. Since the spatial domain is narrow, we reasonably assume stationarity within each local region when aggregating these empirical quantities.

Figures 10 and 11 present model diagnostics based on the first- and second-differenced processes, respectively, across all six reference locations. At each depth level, a single empirical value is computed by aggregating (differenced) observations across all Argo floats within a local region, making use of the assumption of local stationarity. Each bin represents a depth interval of 2 meters. The plotted model estimates (M1, M2, M3) appear as smooth curves per model, consistent with the assumption of horizontal stationarity within each region. M3—our proposed nonstationary cross-covariance model—consistently aligns closely with the empirical estimates in both the first and second differenced diagnostics. This strong agreement confirms that M3

not only captures the colocated correlation on the original scale but also preserves realistic vertical gradients and curvature in the data. By contrast, M1 assumes a constant cross-correlation and produces flat lines across depth, while M2 assumes independence and yields zero correlation throughout. These assumptions visibly misrepresent the empirical behavior, particularly in the second-differenced case. M1 substantially underestimates the magnitude and variation of the empirical curves, most notably at reference locations 2, 3, and 5. Even in the first-differenced case, M1 fails to track the observed structure except in regions where the empirical curve happens to be flat. Notably, at reference location 4, none of the models match the empirical second-difference curve well. This suggests a more complex dependence structure at that site that may not be fully captured by any of the current models and warrants further investigation. Together, these diagnostics validate the robustness of M3 in reproducing depth-varying correlation structures, even after applying differencing operators that amplify local curvature. This capacity to preserve second-order structure under transformation is a strong indication of M3’s fidelity to the true data-generating process.

5 Discussion

Argo floats play a critical role in sampling temperature and salinity throughout the world’s oceans. However, despite the global reach of the Argo network, horizontal and vertical gaps remain. Many locations are undersampled, and vertical resolution is often sparse, with numerous floats not covering the full depth range. In this work, we contributed to the ongoing efforts to produce high-quality interpolations of temperature and salinity at unsampled locations through a bivariate modeling of Argo residuals. Motivated by the underlying physical coupling between temperature and salinity, we extended traditional spatial modeling by incorporating vertical structure—an essential feature of ocean dynamics.

Consistent with findings from previous studies, we showed that the correlation between temperature and salinity varies significantly with depth. Our proposed model captures this vertical

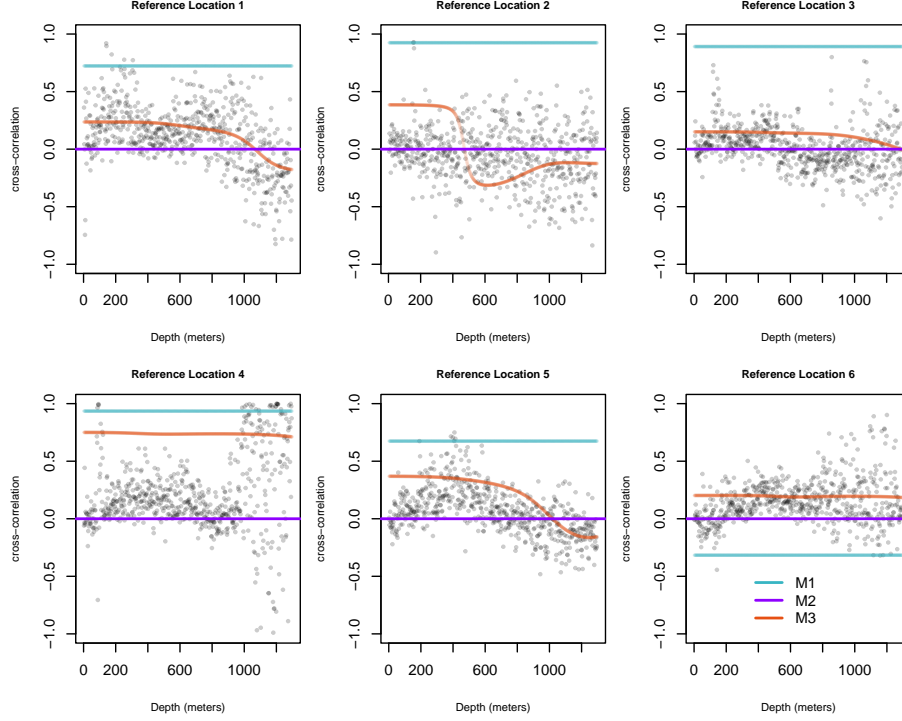


Figure 11: Empirical (black) and model-based estimates of colocated correlations of the second differenced processes, plotted as a function of depth at each reference location.

nonstationarity using a flexible, depth-varying cross-covariance function. The resulting framework accommodates diverse oceanographic conditions and vertical regimes, offering a robust statistical approach for three-dimensional mapping of environmental variables. Building on this foundation, future work could explore extensions such as decoupling cross-covariance parameters from the marginal components or allowing spatial range parameters to vary with depth. Another promising direction is the development of a fully four-dimensional modelling framework that incorporates time as another component, enabling spatiotemporal analysis of oceanographic processes.

References

- Al Senafi, F. and Anis, A. (2020). Internal waves on the continental shelf of the Northwestern Arabian Gulf. *Frontiers in Marine Science*, page 805.
- Alegría, A. (2020). Cross-dimple in the cross-covariance functions of bivariate isotropic random fields on spheres. *Stat*, 9(1):e301.
- Argo, G. (2000). Argo float data and metadata from global data assembly centre (Argo GDAC). *Seanoë*.
- Böhme, L. and Send, U. (2005). Objective analyses of hydrographic data for referencing profiling float salinities in highly variable environments. *Deep Sea Research Part II: Topical Studies in Oceanography*, 52(3-4):651–664.
- Cabanes, C., Thierry, V., and Lagadec, C. (2016). Improvement of bias detection in argo float conductivity sensors and its application in the North Atlantic. *Deep Sea Research Part I: Oceanographic Research Papers*, 114:128–136.
- Cao, J., Guinness, J., Genton, M. G., and Katzfuss, M. (2022). Scalable Gaussian-process regression and variable selection using Vecchia approximations. *Journal of machine learning research*, 23(348):1–30.
- Cao, J., Zhang, J., Sun, Z., and Katzfuss, M. (2024). Locally anisotropic covariance functions on the sphere. *Journal of Agricultural, Biological and Environmental Statistics*, 29:212–231.
- Chaigneau, A., Le Texier, M., Eldin, G., Grados, C., and Pizarro, O. (2011). Vertical structure of mesoscale eddies in the eastern south pacific ocean: A composite analysis from altimetry and argo profiling floats. *Journal of Geophysical Research: Oceans*, 116(C11).
- Chen, G. and Geng, D. (2019). A “mirror layer” of temperature and salinity in the ocean. *Climate Dynamics*, 52(1):1–13.
- Chen, G., Peng, L., and Ma, C. (2018). Climatology and seasonality of upper ocean salinity: a three-dimensional view from Argo floats. *Climate Dynamics*, 50(5):2169–2182.
- Chen, G. and Wang, X. (2016). Vertical structure of upper-ocean seasonality: Annual and semiannual cycles with oceanographic implications. *Journal of Climate*, 29(1):37–59.
- Chen, L., Zhang, R.-H., and Gao, C. (2022). Effects of temperature and salinity on surface currents in the Equatorial Pacific. *Journal of Geophysical Research: Oceans*, 127(4):e2021JC018175.

- Ding, D.-S., Patel, A. K., Singhanian, R. R., Chen, C.-W., and Dong, C.-D. (2022). Effects of temperature and salinity on growth, metabolism and digestive enzymes synthesis of goniopora columna. *Biology*, 11(3):436.
- Dong, C., McWilliams, J. C., Liu, Y., and Chen, D. (2014). Global heat and salt transports by eddy movement. *Nature Communications*, 5(1):1–6.
- Escobar, A., Negro, V., López-Gutiérrez, J. S., and Esteban, M. (2016). Influence of temperature and salinity on hydrodynamic forces. *Journal of Ocean Engineering and Science*, 1(4):325–336.
- Galán, A., Saldías, G. S., Corredor-Acosta, A., Muñoz, R., Lara, C., and Iriarte, J. L. (2021). Argo float reveals biogeochemical characteristics along the freshwater gradient off western patagonia. *Frontiers in Marine Science*, 8:613265.
- Gangopadhyay, A. (2022). *Introduction to Ocean Circulation and Modeling*. CRC Press.
- Gneiting, T., Kleiber, W., and Schlather, M. (2010). Matérn cross-covariance functions for multivariate random fields. *Journal of the American Statistical Association*, 105(491):1167–1177.
- Good, S. A., Martin, M. J., and Rayner, N. A. (2013). En4: Quality controlled ocean temperature and salinity profiles and monthly objective analyses with uncertainty estimates. *Journal of Geophysical Research: Oceans*, 118(12):6704–6716.
- Heaton, M. J., Datta, A., Finley, A. O., Furrer, R., Guinness, J., Guhaniyogi, R., Gerber, F., Gramacy, R. B., Hammerling, D., Katzfuss, M., et al. (2019). A case study competition among methods for analyzing large spatial data. *Journal of Agricultural, Biological and Environmental Statistics*, 24:398–425.
- Helber, R. W., Kara, A. B., Richman, J. G., Carnes, M. R., Barron, C. N., Hurlburt, H. E., and Boyer, T. (2012). Temperature versus salinity gradients below the ocean mixed layer. *Journal of Geophysical Research: Oceans*, 117(C5).
- Hosoda, S., Ohira, T., and Nakamura, T. (2008). A monthly mean dataset of global oceanic temperature and salinity derived from Argo float observations. *JAMSTEC Report of Research and Development*, 8:47–59.
- Hu, A. J., Kuusela, M., Lee, A. B., Giglio, D., and Wood, K. M. (2020). Spatio-temporal methods for estimating subsurface ocean thermal response to tropical cyclones. *arXiv preprint arXiv:2012.15130*.
- Jana, S., Gangopadhyay, A., Haley, P. J., and Lermusiaux, P. F. (2022). Sound speed variability over Bay of Bengal from Argo observations (2011-2020). In *OCEANS 2022-Chennai*, pages 1–8. IEEE.

- Jeong, J., Jun, M., and Genton, M. (2017). Spherical process models for global spatial statistics. *Stat Sci.*, pages 501–513.
- Johnson, G. C., Hosoda, S., Jayne, S. R., Oke, P. R., Riser, S. C., Roemmich, D., Suga, T., Thierry, V., Wijffels, S. E., and Xu, J. (2022). Argo-two decades: global oceanography, revolutionized. *Annual Review of Marine Science*, 14:379–403.
- Jun, M. (2011). Non-stationary cross-covariance models for multivariate processes on a globe. *Scandinavian Journal of Statistics*, 38(4):726–747.
- Jun, M. and Stein, M. L. (2007). An approach to producing space–time covariance functions on spheres. *Technometrics*, 49(4):468–479.
- Jun, M. and Stein, M. L. (2008). Nonstationary covariance models for global data. *The Annals of Applied Statistics*, 2(4):1271–1289.
- Katzfuss, M. and Guinness, J. (2021). A general framework for Vecchia approximations of Gaussian processes. *Statistical Science*, 36(1):124–141.
- Kleiber, W. and Genton, M. G. (2013). Spatially varying cross-correlation coefficients in the presence of nugget effects. *Biometrika*, 100(1):213–220.
- Kleiber, W. and Nychka, D. (2012). Nonstationary modeling for multivariate spatial processes. *Journal of Multivariate Analysis*, 112:76–91.
- Kunoth, A., Lyche, T., Sangalli, G., Serra-Capizzano, S., Lyche, T., Manni, C., and Speleers, H. (2018). Foundations of spline theory: B-splines, spline approximation, and hierarchical refinement. *Splines and PDEs: From Approximation Theory to Numerical Linear Algebra: Cetraro, Italy 2017*, pages 1–76.
- Kuusela, M. and Stein, M. L. (2018). Locally stationary spatio-temporal interpolation of Argo profiling float data. *Proceedings of the Royal Society A*, 474(2220):20180400.
- Li, H., Xu, F., Zhou, W., Wang, D., Wright, J. S., Liu, Z., and Lin, Y. (2017). Development of a global gridded Argo data set with Barnes successive corrections. *Journal of Geophysical Research: Oceans*, 122(2):866–889.
- Liu, C., Liang, X., Chambers, D. P., and Ponte, R. M. (2020a). Global patterns of spatial and temporal variability in salinity from multiple gridded Argo products. *Journal of Climate*, 33(20):8751–8766.
- Liu, H., Ong, Y.-S., Shen, X., and Cai, J. (2020b). When Gaussian process meets big data: A review of scalable GPs. *IEEE transactions on neural networks and learning systems*, 31(11):4405–4423.

- Maes, C. and O’Kane, T. J. (2014). Seasonal variations of the upper ocean salinity stratification in the tropics. *Journal of Geophysical Research: Oceans*, 119(3):1706–1722.
- McPhaden, M. J. and Hayes, S. P. (1991). On the variability of winds, sea surface temperature, and surface layer heat content in the western equatorial Pacific. *Journal of Geophysical Research: Oceans*, 96(S01):3331–3342.
- Merchel, M., Walczowski, W., Rak, D., and Wieczorek, P. (2024). The use of Argo floats as virtual moorings for monitoring the South Baltic Sea. *Oceanologia*, 66(1):99–110.
- Olson, S., Jansen, M. F., Abbot, D. S., Halevy, I., and Goldblatt, C. (2022). The effect of ocean salinity on climate and its implications for Earth’s habitability. *Geophysical Research Letters*, 49(10):e2021GL095748.
- Pawlowicz, R. (2013). Key physical variables in the ocean: temperature, salinity, and density. *Nature Education Knowledge*, 4(4):13.
- Roemmich, D. and Gilson, J. (2009). The 2004–2008 mean and annual cycle of temperature, salinity, and steric height in the global ocean from the Argo program. *Progress in Oceanography*, 82(2):81–100.
- Sambe, F. and Suga, T. (2022). Unsupervised clustering of Argo temperature and salinity profiles in the mid-latitude Northwest Pacific Ocean and revealed influence of the Kuroshio extension variability on the vertical structure distribution. *Journal of Geophysical Research: Oceans*, 127(3):e2021JC018138.
- Vecchia, A. V. (1988). Estimation and Model Identification for Continuous Spatial Processes. *Journal of the Royal Statistical Society. Series B (Methodological)*, 50(2):297–312. Publisher: [Royal Statistical Society, Wiley].
- Walker, R. H., Smith, G. D., Hudson, S. B., French, S. S., and Walters, A. W. (2020). Warmer temperatures interact with salinity to weaken physiological facilitation to stress in freshwater fishes. *Conservation Physiology*, 8(1):coaa107.
- Wang, T., Gille, S. T., Mazloff, M. R., Zilberman, N. V., and Du, Y. (2020). Eddy-induced acceleration of argo floats. *Journal of Geophysical Research: Oceans*, 125(10):e2019JC016042.
- Wong, A. P., Wijffels, S. E., Riser, S. C., Pouliquen, S., Hosoda, S., Roemmich, D., Gilson, J., Johnson, G. C., Martini, K., Murphy, D. J., et al. (2020). Argo data 1999–2019: two million temperature-salinity profiles and subsurface velocity observations from a global array of profiling floats. *Frontiers in Marine Science*, page 700.
- Xie, S.-P., Kunitani, T., Kubokawa, A., Nonaka, M., and Hosoda, S. (2000). Interdecadal thermocline variability in the North Pacific for 1958–97: A GCM simulation. *Journal of Physical Oceanography*, 30(11):2798–2813.

Yarger, D., Stoev, S., and Hsing, T. (2022). A functional-data approach to the Argo data. *The Annals of Applied Statistics*, 16(1):216–246.

Appendix

A Assessment of Gaussianity Assumption

To evaluate the Gaussianity assumption, we examine the distribution of temperature and salinity residuals across six reference locations and five depth layers (0–100 m, 100–500 m, 500–1000 m, 1000–1500 m, and 1500–2000 m). Figures A.1 and A.2 present corresponding histograms and Q–Q plots for each location and depth bin. Overall, residuals are approximately Gaussian, with better conformity in deeper layers. Shallow regions show some deviations—such as skewness or heavy tails—likely due to surface variability, stratification, or unresolved mesoscale dynamics. These deviations diminish with depth, suggesting improved homogeneity and model fit at lower layers. Importantly, none of the departures are severe enough to undermine the Gaussian modeling assumption used in kriging and inference.

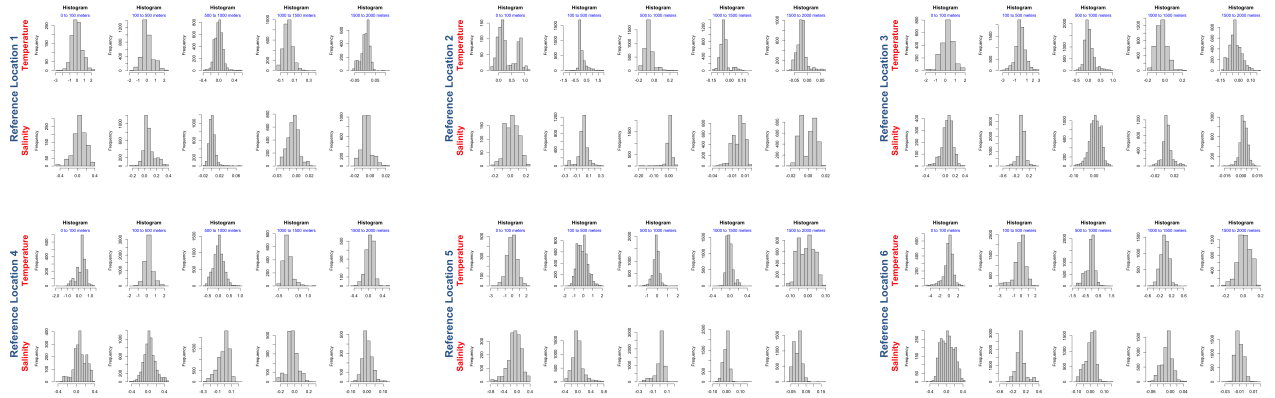


Figure A.1: Histograms of standardized temperature (top row) and salinity (bottom row) residuals across five depth intervals for each of the six reference locations.

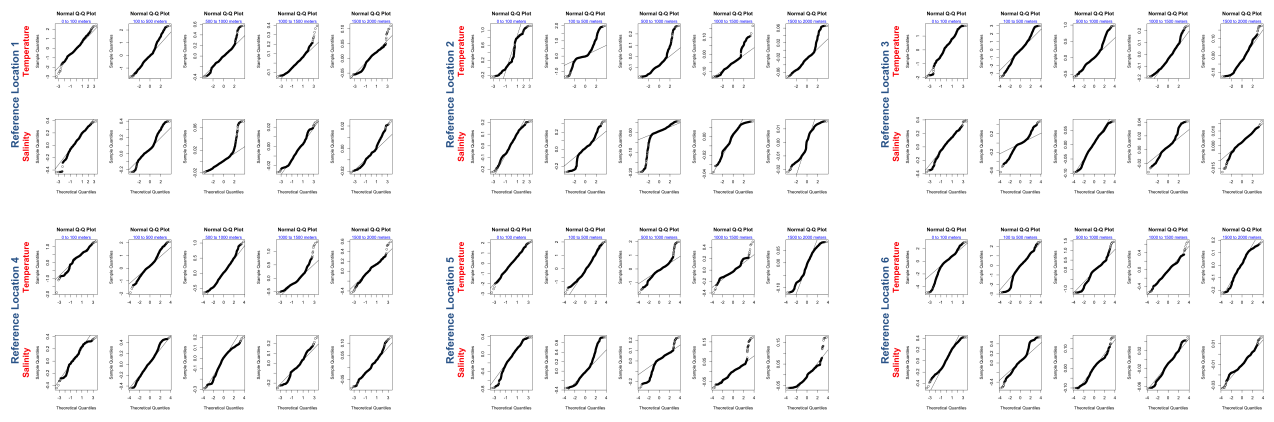


Figure A.2: Q-Q plots of standardized temperature (top row) and salinity (bottom row) residuals across five depth intervals for each of the six reference locations.